

The Rheology of Soft Bodies Suspended in the Simple Shear Flow of a Viscoelastic Fluid

Christopher J. Guido^a, Eric S. G. Shaqfeh^{a,b,c,*}

^a Department of Chemical Engineering, Stanford University, Stanford, CA 94305, USA

^b Department of Mechanical Engineering, Stanford University, Stanford, CA 94305, USA

^c Institute for Computational and Mathematical Engineering, Stanford University, Stanford, CA 94305, USA

ARTICLE INFO

Keywords:

Rheology

Viscoelasticity

Soft particles

Immersed boundary methods

ABSTRACT

Many industrial applications involve soft suspended bodies in viscoelastic fluids. Moreover, many biological fluids contain high molecular weight macromolecules which impart viscoelasticity to the fluid, and any cells which are suspended in such fluids again form a suspension of elastic bodies in a viscoelastic fluid. For control purposes, microfluidic platforms are beginning to utilizing viscoelastic solvents to perform tasks such as cell focusing [34]. However, despite numerical studies into the kinematics of such deformable bodies in viscoelastic fluids, no studies currently consider the rheology of such systems. Due to the competing effects of the viscoelasticity of the fluid and the elasticity of the solids it is clear that there exists a non-trivial rheological behavior exhibited by such suspensions. In this study, we present simulations of dilute systems of deformable particles with viscoelastic suspending fluids. We compute the effective viscosity and the first/second normal stresses for a suspension of neo-Hookean particles sheared in a Giesekus suspending fluid up to modest deformations characterized by a capillary number, Ca , up to $Ca = 0.3$. The results indicate that the per particle extra stress that originates from the suspending fluid (the particle induced fluid stress) remains relatively constant regardless of deformation. In contrast, the component of the extra stress that arises from the stress inside the particle (the stresslet) is a strong function of both the capillary number and the Weissenberg number for the parameter space investigated. Note that we find the suspensions "thicken" and/or "thin" with increasing shear depending on the range of parameter space examined.

1. Introduction


A considerable number of fluids in industrial and biological applications are viscoelastic in nature. These fluids often have suspended large polymeric molecules and contain suspended additives which may demonstrate non-trivial elasticity [4]. In biological applications, such as when cells are suspended, the soft particulates generally demonstrate non-negligible elasticity and this creates non-trivial modeling challenges even in Newtonian fluids [32]. The rheological behavior of suspensions containing elastic particles is central to the design of many microfluidic devices, which can be used for both diagnostic and health applications. Recently, adding viscoelastic fluids to cellular suspensions has been shown to aid in the design of cell focusing microfluidic technologies, demonstrating the need to further understand the rheology of suspensions of soft particles that are suspended in viscoelastic fluids [34].

A number of numerical approaches have been developed to study particles suspended in Newtonian and viscoelastic flows. For rigid particles in Newtonian flows, both spherical and non-spherical particles have been considered through numerous methods including immersed boundary techniques and body fitted techniques such as the boundary element method (BEM) [22, 27, 1, 31]. Additionally, numerical simulations of interesting dynamic behavior of rigid particles while suspended in viscoelastic fluids have been demonstrated in many publications [9, 23, 46, 7, 8]. These studies gen-

erally remove the suspended particle elasticity as a serious contributing factor, but a rich dynamic behavior is still exhibited by these suspensions. Particles exhibit novel migration in the Poiseuille flow of a viscoelastic fluid and non-spherical particles have been shown to achieve steady fixed orientations in shear flows where in Newtonian fluids we would expect steady orbits [9, 23, 46, 7, 8]. Collisions between rigid particles and walls have also been considered for viscoelastic fluids through numerical methods [2]. A final interesting dynamic behavior that has been considered for suspensions in viscoelastic fluids is particle chaining. This has been simulated numerically for 2D systems [16, 17]. Note this all suggests that the physics of deformable particles in viscoelastic fluids is even more rich. However, to examine these systems, the aforementioned numerical methods above need to be redeveloped to include suspended particle deformation and elasticity.

Some tools do exist for studying deformable particles in viscoelastic and Newtonian flows. In Newtonian fluids immersed finite element methods have been implemented for solid particles with finite elasticity [53, 54]. Additionally, a host of immersed boundary and boundary element methods have been utilized for capsules (infinitely thin sacks with fluid inside and outside) [10, 3, 32, 30, 36, 44, 25, 26]. In viscoelastic fluids, methods including immersed boundary methods for capsules have been developed but no extensions to soft solid bodies have been presented [34, 33]. Eulerian based methods have also been used with considerable success for deformable particles with a variety of constitutive models [45, 40, 39, 15]. Deformable particles in viscoelas-

*Corresponding author

 esgs@stanford.edu.org (E.S.G. Shaqfeh)

ORCID(s): 0000-0003-4876-6673 (C.J. Guido)

tic flows have also been studied using body-fitted methods in simple shear and pressure driven flows [47, 48, 49]. However to date, no such studies have considered the effective rheology of such suspensions of viscoelastic fluids with elastic particles. In the present manuscript, we consider this rheology problem in simple shear, utilizing a previously published immersed boundary method to study dilute systems of suspended deformable particles [41].

Note that one of the reasons that previous researchers did not examine the effective rheology of these suspensions is that the theory surrounding how to calculate such effective properties was being developed. And indeed, recently, a number of researchers have correctly calculated the rheological effects of particle additives to viscoelastic fluids when the particulates are very rigid. These studies have concluded that there is a rich rheological behavior primarily associated with the effects by the particles on the suspending fluid. The particle will cause shear thickening due to the increased stress in the fluid surrounding the particle despite the fact that the average stress in the particle actually decreases [50, 52, 51]. The contribution to the extra stress in the suspension can thus be broken into two distinct parts: the stresslet and the particle induced fluid stress (PIFS). The stresslet is the additional extra stress found within the particle, and this is the integral measure that is most often calculated in Newtonian suspensions. The PIFS is the extra stress created in the fluid due to the disturbance created by the particle; for Newtonian fluids this is always zero. In simple shear flow, it has been found that the PIFS contribution to the effective viscosity steadily increases as the elasticity (Weissenberg number) of the fluid increases while the stresslet is found to decrease. This ultimately leads to an overall shear-thickening effect when particles are added to a viscoelastic suspending fluid in shear flow [50, 51]. Additionally, these results for dilute suspensions have been considered analytically via a number of perturbation techniques which all agree with the results presented in the numerical simulations [11, 35, 19, 20, 18]. These numerical studies have also been extended to examine the effects of multiple particle interactions in non-dilute suspensions [21, 52]. These non-dilute suspensions show the interesting scalings with the particle volume fraction. Since most of the extra stress is in a small region confined to the near particle surface, that scaling of the viscometrics in the volume fraction collapse up to a considerable volume fraction of about 5% [52]. These systems have also been considered experimentally, and the results of the simulations discussed above show qualitative agreement with the experimental behavior of these suspensions [6, 42, 43].

Note that the rheology of elastic particles suspended in Newtonian flows have been considered through a number of studies. A simple perturbation expansion for the shape of an elastic particle in shear was conducted in 1981 by Murata *et al.* [28]. A different analysis by Roscoe *et al.* considered the shape and rheology of deformable particles within certain approximations [38]. The current state of the art analytical result was calculated by Gao *et al.* who determined

both the shape and the viscometrics for single initially spherical deformable particles using a polarization technique [12]. The viscometrics in these suspensions (i.e. elastic particles in Newtonian suspending fluids) behave in a way that runs counter to that described above for rigid particles in viscoelastic fluids. The effective viscosity of soft particles in Newtonian suspending fluids drop as particles get softer and the the normal stresses grow nearly linearly with the elasticity parameter (the capillary number). Similar results have been calculated for capsules numerically for both dilute and dense suspensions, which suggests that capsules and solid deformable particles in Newtonian flows behave similarly at least qualitatively [5, 24].

Due to the competing effects of the capillarity (associated with particle deformation) and the viscoelasticity of the suspending fluid there is clearly an interesting problem when the two features are combined in a soft particle suspension. In this work, we will consider simulations of dilute suspensions of deformable particles with a viscoelastic suspending fluid using an immersed boundary formulation [41]. The viscometrics will be explored as a function of the material parameters (the capillary number and the Weissenberg number) and we will compare and contrast these results for soft particles to the previous results for rigid particle suspensions.

2. Methodology

2.1. Governing Equations

We consider the problem of an incompressible suspended elastic body in an incompressible Newtonian or viscoelastic fluid under shear flow. Additionally, the particle will be considered to be neutrally buoyant so that the density is constant throughout both phases. The domain of consideration can be broken into two parts defined to be Ω^f and Ω^s which represent the volume of the liquid and the solid respectively. We have illustrated this domain below in Fig. 1. The particle in flow and the appropriate variables that will be discussed in the remainder of this paper have been illustrated.

We will refer to the total domain including both the particle and the liquid to be Ω . For both phases the equations are conservation of momentum as well as continuity (which can be expressed similarly in both sub-domains):

$$\rho \frac{D\mathbf{v}}{Dt} = \nabla \cdot \boldsymbol{\sigma}^f \quad x \in \Omega^f, \quad (1)$$

$$\rho \frac{D\mathbf{v}}{Dt} = \nabla \cdot \boldsymbol{\sigma}^s \quad x \in \Omega^s, \quad (2)$$

$$\nabla \cdot \mathbf{v} = 0 \quad x \in \Omega^s, \Omega^f. \quad (3)$$

Note that because of Eq. 3, we are restricted to considering incompressible solid objects and suspending fluids. We have defined the stress in the solid and liquid to be $\boldsymbol{\sigma}^s$ and $\boldsymbol{\sigma}^f$ respectively. At the boundary of contact between the solid and the liquid we also require a stress balance to be satisfied. We denote this boundary as $\partial\Omega^s$ with an outwardly-pointing unit normal \mathbf{n} . We write this condition as

$$(\boldsymbol{\sigma}^s - \boldsymbol{\sigma}^f) \cdot \mathbf{n} = 0 \quad x \in \partial\Omega^s. \quad (4)$$

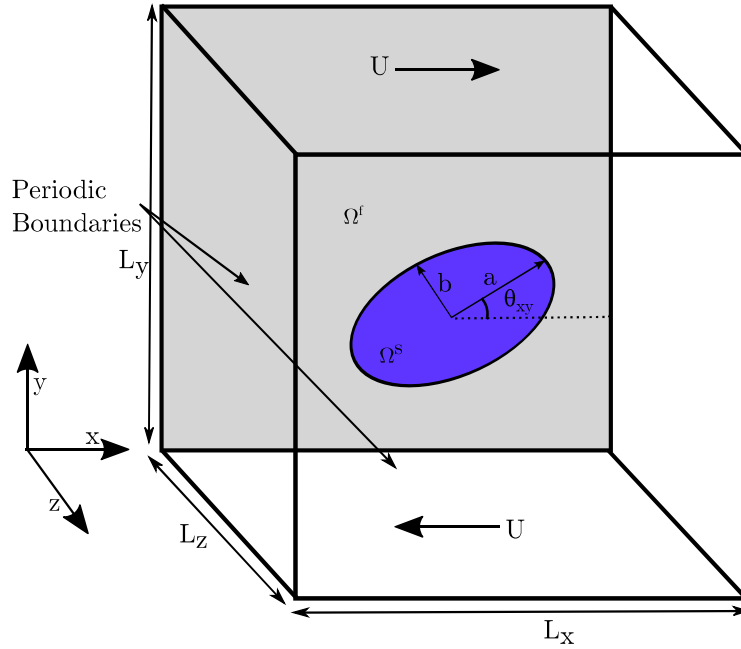


Figure 1: The domain for a suspended elastic particle in shear. The domain is of finite size with domain lengths L_x , L_y , and L_z in each direction. For the dilute simulations we utilize a box size of $5 \times 5 \times 5D_p$ where D_p is the particle diameter initially. The particle is illustrated in a deformed state with major and minor axis lengths a and b respectively inclined at an angle θ_{xy} . The shear flow is applied at the y boundaries by applying a boundary velocity U so that the applied shear rate is $\dot{\gamma} = \frac{2U}{L_y}$. The x and z boundaries are periodic in our simulations. The solid domain will be referred to as Ω^s and the fluid domain is Ω^f . The total combined domain is $\Omega = \Omega^f + \Omega^s$.

To model a viscoelastic, polymeric suspending medium, we represent the suspending liquid stress as a sum of a Newtonian stress with an additional polymeric stress,

$$\boldsymbol{\sigma}^f = \boldsymbol{\sigma}^N + \boldsymbol{\sigma}^P = -p\mathbf{I} + \eta \left(\frac{\partial \mathbf{v}}{\partial \mathbf{x}} + \frac{\partial \mathbf{v}^T}{\partial \mathbf{x}} \right) + \boldsymbol{\sigma}^P. \quad (5)$$

Above, we have defined p to be the hydrodynamic pressure and η to be the Newtonian fluid viscosity. We describe the extra polymer stress, $\boldsymbol{\sigma}^P$, using the Giesekus model [13, 4] which describes the evolution of the extra stress through a conformation tensor \mathbf{C} and a relaxation time λ ,

$$\boldsymbol{\sigma}^P = \frac{\eta_p}{\lambda}(\mathbf{C} - \mathbf{I}), \quad (6)$$

$$\lambda \overset{\nabla}{\mathbf{C}} + (\mathbf{C} - \mathbf{I}) + \alpha(\mathbf{C} - \mathbf{I})^2 = 0. \quad (7)$$

In Eqn. 7, $\overset{\nabla}{\mathbf{C}}$ is the upper-convected time derivative and in Eqn. 6 we have defined η_p to be the polymeric viscosity. The Giesekus constitutive equation considers the individual polymer molecules to be Hookean dumbbells, allowing for anisotropic drag via the Giesekus mobility parameter α . The Oldroyd-B model is recovered from the Giesekus model if $\alpha = 0$. The Oldroyd-B model, however, displays no shear thinning, which is a common feature of many polymeric fluids so we will utilize the Giesekus model for our rheological studies. In either case, the zero shear viscosity of the suspending fluid is

$$\eta_0 = \eta + \eta_p. \quad (8)$$

We also must determine the stress in the solid phase, $\boldsymbol{\sigma}^s$. There are multiple appropriate stress definitions and the relations between them are presented below. The first Piola-Kirchhoff stress, \mathbf{P} , can be obtained from the Cauchy stress tensor, $\boldsymbol{\sigma}$, the deformation gradient, \mathbf{F} , and $J = \det(\mathbf{F})$ using the identity $\mathbf{P} = J\boldsymbol{\sigma} \cdot \mathbf{F}^{-T}$. The Cauchy stress, $\boldsymbol{\sigma}$, is related to the second Piola-Kirchhoff stress, \mathbf{S} , using $\boldsymbol{\sigma} = \frac{1}{J}\mathbf{F} \cdot \mathbf{S} \cdot \mathbf{F}^T$. We also can construct the right Cauchy-Green tensor $\mathbf{C} = \mathbf{F}^T \mathbf{F}$ which has three spatial invariants I_1^C, I_2^C , and I_3^C .

\mathbf{S} is calculated using the principle of virtual work as:

$$\mathbf{S} = 2 \frac{\partial W}{\partial \mathbf{C}} = 2 \left\{ \left(\frac{\partial W}{\partial I_1^C} + I_1^C \frac{\partial W}{\partial I_2^C} \right) \mathbf{I} - \mathbf{C} \frac{\partial W}{\partial I_2^C} + I_3^C \mathbf{C}^{-1} \frac{\partial W}{\partial I_3^C} \right\}. \quad (9)$$

For the deformable solid we utilize a slightly compressible neo-Hookean model with bulk modulus λ_p and shear modulus μ_p so the strain energy density, W , becomes:

$$W = \frac{\lambda_p}{4}(I_3^C - 1) - \left(\frac{\lambda_p}{2} + \mu_p \right) \ln(I_3^C)^{1/2} + \frac{\mu_p}{2}(I_1^C - 3). \quad (10)$$

2.2. Numerical Implementation

To solve the coupled fluid-solid problem we utilize an Immersed Finite Element Method (IFEM) that has been outlined in a previous paper [41]. For completeness the algorithm will be summarized briefly.

To arrive at the governing equations for this method, we rewrite Eqns. 1 and 2 as a single equation over the total domain as follows:

$$\rho_f \frac{D\mathbf{v}}{Dt} = \nabla \cdot \boldsymbol{\sigma}^f + \mathbf{f}^{\text{IB}} \quad x \in \Omega, \quad (11)$$

where \mathbf{f}^{IB} is the immersed boundary force density. It is clear that for conservation of momentum to be satisfied everywhere, the immersed boundary force density must take the following form:

$$\mathbf{f}^{\text{IB}} = \nabla \cdot (\boldsymbol{\sigma}^s - \boldsymbol{\sigma}^f) \quad x \in \Omega^s. \quad (12)$$

The discretized IFEM method utilizes two separate grids. The Lagrangian grid (LG) tracks the particles (Ω^s) while a second fixed Eulerian grid (EUL) is utilized for the entire domain ($\Omega^s + \Omega^f = \Omega$). We utilize a finite volume method to solve for all quantities on the Eulerian grid and finite elements (linear tetrahedral elements) to solve for the forces on the Lagrangian grid. Since forces, velocities, and conformation tensor components will need to be shared between these two grids for any of these calculations, interpolation and spreading operators are required. We will define an operator S^h to be the interpolation operator from EUL to LG and S^{*h} to be the inverse operator.

It is worth noting that mesh resolution for the LG grid needs to be carefully selected to ensure that 'leaking' is avoided. In the context of the IFEM, 'leaking' refers to an LG grid that is too sparse (especially when heavily deformed) which leads to the spreading of forces that are not continuous in nature near the boundary of the solid object. This almost always leads to an unstable solution. To ensure that this does not occur, we ensure that all of our initial meshes are sufficiently fine such that the final deformed mesh does not exhibit this undesirable 'leaking' behavior.

We distinguish between the immersed boundary force on the Lagrangian grid and the immersed boundary force in the Eulerian domain which are defined to be $\mathbf{F}^{\text{IB},s}$ and $\mathbf{F}^{\text{IB},f}$ respectively (Note that force densities are given by a lowercase \mathbf{f} and forces are given by uppercase \mathbf{F}).

On the Eulerian domain we therefore solve the following expression with a third order accurate finite volume scheme developed at Stanford's Center for Turbulence research [14]:

$$\rho \frac{D\mathbf{v}}{Dt} = \nabla \cdot \boldsymbol{\sigma}^f + \mathbf{f}^{\text{IB},f} = \nabla \cdot \boldsymbol{\sigma}^f + S^* [\mathbf{f}^{\text{IB},s}] \quad x \in \Omega. \quad (13)$$

If we desire to include viscoelasticity in our simulation, we solve for the conformation tensor \mathbf{C} as six scalar equations (since \mathbf{C} is symmetric) using a log-conformation method. Details about this method can be found in previous papers by members of our group [50, 37, 29].

We are left to determine the values of $\mathbf{F}^{\text{IB},s}$ for which we utilize finite elements. If we multiply Eqn. 12 by a test function \mathbf{w} and integrate over the solid body then we retrieve:

$$\int_{\Omega^s} \mathbf{f}_i^{\text{IB},s} w_i d\Omega = \int_{\Omega^s} \nabla_j (\sigma_{ij}^s - \sigma_{ij}^f) w_i d\Omega \quad \in \Omega^s. \quad (14)$$

Through a series of manipulations we can arrive at the final form of this expression for the force discretely at each node k :

$$\mathbf{F}_{k,i}^{\text{IB},s} = - \int_{\Omega_0^s} (P_{ij}^s - P_{ij}^f) \nabla_j N_k d\Omega. \quad (15)$$

Note that in the above expression we have a total of three contributions to the force if we divide the fluid contribution into Newtonian and polymer contributions (using Eqn. 5):

$$\mathbf{F}_{k,i}^{\text{IB},s} = - \int_{\Omega_0^s} (P_{ij}^s - P_{ij}^{f,N} - P_{ij}^{f,P}) \nabla_j N_k d\Omega. \quad (16)$$

To calculate the values of $P_{ij}^{f,N}$ and $P_{ij}^{f,P}$ on the Lagrangian grid, the values of \mathbf{v} and \mathbf{C} must be known at each Lagrangian point. These values are therefore required to be interpolated from the Eulerian grid. Thus, the total immersed boundary force can be broken into an elastic, Newtonian, and polymer components:

$$\mathbf{F}_k^{\text{IB}} = \mathbf{F}_k^{\text{el}} + \mathbf{F}_k^{\text{N}} + \mathbf{F}_k^{\text{P}}. \quad (17)$$

The discrete calculation of P_{ij}^s , $P_{ij}^{f,N}$, and $P_{ij}^{f,P}$ is conducted on the Lagrangian mesh on the reference configuration. For solid particles we utilize a 4-node tetrahedral mesh which allows us to discretely write the deformation gradient ($F_{ij}^{\Omega_e}$) and velocity gradient on each element of this mesh. The values of the deformation gradient and the velocity gradient are constant over each element volume Ω_e on the reference configuration and can be written as:

$$F_{ij}^{\Omega_e} = \sum_{k=1}^4 x_{i,k} \nabla_j N_k, \quad (18)$$

$$\left(\frac{\partial u_i}{\partial x_j} \right)^{\Omega_e} = \sum_{k=1}^4 u_{i,k} \nabla_j N_k F_{lj}^{-1,\Omega_e}. \quad (19)$$

In the above expressions $x_{i,k}$ and $u_{i,k}$ are the position and velocity of at each node k on the current configuration (on Ω^s). These quantities can then be used to construct the stresses over each element discretely as:

$$\begin{aligned} P_{ij}^{\Omega_e} &= F_{ik}^{\Omega_e} S_{kj}^{\Omega_e} \\ &= F_{ik}^{\Omega_e} \left(\frac{\lambda_p}{2} (J^2 - 1) F_{kl}^{-1,\Omega_e} F_{lj}^{-T,\Omega_e} \right. \\ &\quad \left. + \mu_p (\delta_{kj} - F_{kl}^{-1,\Omega_e} F_{lj}^{-T,\Omega_e}) \right) \end{aligned} \quad (20)$$

$$P_{ij}^{f,N,\Omega_e} = \eta J \left(\left(\frac{\partial u_i}{\partial x_k} \right)^{\Omega_e} + \left(\frac{\partial u_k}{\partial x_i} \right)^{\Omega_e} \right) F_{kj}^{\Omega_e, -T}. \quad (21)$$

Since the conformation tensor has been directly interpolated to the grid, P_{ij}^{f,P,Ω_e} can be calculated as:

$$P_{ij}^{f,P,\Omega_e} = \sum_{k=1}^4 J \frac{\eta(1-\beta)}{\lambda} \frac{(C_{il,k} - \delta_{il})}{4} F_{lj}^{\Omega_e, -T}. \quad (22)$$

These quantities can then be utilized to evaluate the integral expressed in Eqn. 15. Following the completion of a time step the Lagrangian mesh is updated using the interpolated velocities via an Adams-Bashforth scheme:

$$\mathbf{x}_k^{s,n+1} = \mathbf{x}_k^{s,n} + \Delta t \left(\frac{3}{2} \mathbf{v}_k^{s,n} - \frac{1}{2} \mathbf{v}_k^{s,n-1} \right).$$

2.3. Non-dimensional Equations

We can write all of the governing equations in a standard non-dimensional form. We chose the characteristic length to be that of the particle D_p , the characteristic time scale to be $\dot{\gamma}$ (The shear rate in the applied flow), the characteristic stress in the fluid to be the $\eta\dot{\gamma}$, the characteristic stress in the particle to be μ_p . This gives us the following non-dimensional equations to solve (where non-dimensional variables and operators are given a bar):

$$\begin{aligned} \text{Re} \frac{D\bar{\mathbf{v}}}{D\bar{t}} &= \bar{\nabla} \cdot \bar{\boldsymbol{\sigma}}^f = \\ &- \bar{\nabla} \bar{p} + \beta \bar{\nabla}^2 \bar{\mathbf{v}} + \frac{1-\beta}{\text{De}} \bar{\nabla} \cdot (\mathbf{C} - \mathbf{I}) \quad x \in \Omega^f, \end{aligned} \quad (23)$$

$$\text{Re} \frac{D\bar{\mathbf{v}}}{D\bar{t}} = \frac{1}{\text{Ca}} \bar{\nabla} \cdot \bar{\boldsymbol{\sigma}}^s \quad x \in \Omega^s, \quad (24)$$

$$\bar{\nabla} \cdot \bar{\mathbf{v}} = 0 \quad x \in \Omega, \quad (25)$$

$$\text{Wi} \bar{\mathbf{C}} + (\mathbf{C} - \mathbf{I}) + \alpha(\mathbf{C} - \mathbf{I})^2 = 0. \quad (26)$$

We also have the following non-dimensional energy density relationship in the solid:

$$\begin{aligned} \hat{W} &= \frac{\lambda_p}{4\mu_p} (I_3^C - 1) \\ &- \left(\frac{\lambda_p}{2\mu_p} + 1 \right) \ln(I_3^C)^{1/2} + \frac{1}{2} (I_1^C - 3). \end{aligned} \quad (27)$$

We can construct a total of 9 dimensionless parameters: The Reynold's number ($\text{Re} = \frac{\rho\dot{\gamma}D_p}{\eta_0}$), the Weissenberg Number ($\text{Wi} = \lambda\dot{\gamma}$) the viscoelastic viscosity ratio ($\beta = \frac{\eta}{\eta+\eta_p}$), the mobility parameter (α), and the capillary number ($\text{Ca} = \frac{\eta_0\dot{\gamma}}{\mu_p}$) appear in the evolution equations. Additionally, a ratio appears in the constitutive equations for the solids: $\frac{\lambda_p}{\mu_p}$. Lastly, the three confinement ratios can be constructed from the geometric parameters ($\frac{D_p}{L_x}, \frac{D_p}{L_y}, \frac{D_p}{L_z}$).

For the studies presented in this paper the Reynold's number will be smaller than 10^{-1} , but the capillary number and

the Weissenberg number will be free to vary. The capillary number quantifies the deformability of the particle and the Weissenberg number quantifies the elasticity of the fluid.

We also set the dimensionless parameter $\frac{\lambda_p}{\mu_p}$ to be sufficiently large that it does not effect any calculated results for all of our simulations presented in this study. The confinement parameters will all be set to 0.2 in this paper unless otherwise noted.

2.4. Calculation of Viscometrics and Shape Parameters

When examining particles in shear flow there are a series of parameters that we calculate both related to the particles shape and to the viscometrics. The particles shape will largely be considered for validation purposes as this has been explored in previous publications [12]. The two deformation parameters that are of interest are the Taylor Deformation parameter (D) and the inclination angle (θ). For an ellipsoidal particle with major axis a and minor axis b in the xy plane, the Taylor deformation number is defined as:

$$D = \frac{a-b}{a+b}. \quad (28)$$

The major and minor axes a and b are determined in two steps: first, the moment of an inertia of the capsule is calculated using the relation [36, 5]:

$$\mathbf{I}_p = \frac{1}{5} \sum_I [(\mathbf{x}_I^s \cdot \mathbf{x}_I^s) (\mathbf{x}_I^s \cdot \mathbf{n}_I) \mathbf{I} - \mathbf{x}_I^s \mathbf{x}_I^s (\mathbf{x}_I^s \cdot \mathbf{n}_I)]. \quad (29)$$

and then an ellipsoidal body is found with the equivalent moment of inertia which requires finding the eigenvalues of \mathbf{I}_p . Specifically, a and b are found as the knowns of three analytical equations which relates the eigenvalues of \mathbf{I}_p to the 3 components of the moment of inertia for a perfect ellipsoid. The inclination angle is similarly calculated from these eigenvalues.

We also need to calculate viscometrics. We define the dimensionless volume average stress in a suspension to be the following:

$$\begin{aligned} \langle \bar{\boldsymbol{\sigma}} \rangle &= \frac{1}{V} \frac{\int_{\Omega} \boldsymbol{\sigma} d\Omega}{\eta_0 \dot{\gamma}} \\ &= \frac{1}{V} \frac{\int_{\Omega^f} \boldsymbol{\sigma}^f d\Omega^f}{\eta_0 \dot{\gamma}} + \frac{1}{V} \frac{\int_{\Omega^s} \boldsymbol{\sigma}^s d\Omega^s}{\eta_0 \dot{\gamma}}. \end{aligned} \quad (30)$$

We can rewrite this expression as an integral over the total domain and the particle domain:

$$\langle \bar{\boldsymbol{\sigma}} \rangle = \frac{1}{V} \frac{\int_{\Omega} \boldsymbol{\sigma}^f dV}{\eta_0 \dot{\gamma}} + \frac{1}{V} \frac{\int_{\Omega^s} (\boldsymbol{\sigma}^s - \boldsymbol{\sigma}^f) d\Omega^s}{\eta_0 \dot{\gamma}}. \quad (31)$$

If we are interested in the per particle contribution to the stress than we can rewrite the expression:

$$\begin{aligned} \langle \bar{\boldsymbol{\sigma}} \rangle &= \langle \bar{\boldsymbol{\sigma}}^{f0} \rangle \\ &+ \frac{\int_{\Omega} (\boldsymbol{\sigma}^f - \boldsymbol{\sigma}^{f0}) dV}{\eta_0 \dot{\gamma}} + \frac{\int_{\Omega^s} (\boldsymbol{\sigma}^s - \boldsymbol{\sigma}^f) d\Omega^s}{\eta_0 \dot{\gamma}}. \end{aligned} \quad (32)$$

Here, the fluid stress if the particle were absent in the flow is defined as σ^{f0} . We can further re-write this expression, using the particle volume fraction ϕ , as:

$$\langle \bar{\sigma} \rangle = \langle \bar{\sigma}^{f0} \rangle + \phi \Sigma + \phi S. \quad (33)$$

Which gives us the following:

$$\Sigma = \frac{\int_{\Omega} (\sigma^f - \sigma^{f0}) dV}{\eta_0 \dot{\gamma} \phi}, \quad (34)$$

$$S = \frac{\int_{\Omega^s} (\sigma^s - \sigma^f) d\Omega^s}{\eta_0 \dot{\gamma} \phi}. \quad (35)$$

In the above expressions we have defined the particle induced fluid stress to be Σ and the stresslet to be S . In previous work these quantities have been defined in this same manner modulo a factor of $\frac{4\pi}{3}$, but we will utilize the above definitions throughout this study [50, 51]. The standard relative non-dimensional viscometric functions on a per-particle basis will be presented in this study and these are defined as follows:

$$\mu_{\text{eff}} = \frac{\langle \sigma_{12} \rangle - \langle \sigma_{12}^{f0} \rangle}{\eta_0 \dot{\gamma} \phi}, \quad (36)$$

$$\Pi_1 = \frac{\langle \sigma_{11} \rangle - \langle \sigma_{22} \rangle - (\langle \sigma_{11}^{f0} \rangle - \langle \sigma_{22}^{f0} \rangle)}{\eta_0 \dot{\gamma} \phi}, \quad (37)$$

$$\Pi_2 = \frac{\langle \sigma_{22} \rangle - \langle \sigma_{33} \rangle - (\langle \sigma_{22}^{f0} \rangle - \langle \sigma_{33}^{f0} \rangle)}{\eta_0 \dot{\gamma} \phi}. \quad (38)$$

Lastly, we define the first and second normal stress coefficients which will be discussed briefly when comparing to previous work with rigid particles:

$$\Psi_1 = \frac{\Pi_1}{Wi}, \quad (39)$$

$$\Psi_2 = \frac{\Pi_2}{Wi}. \quad (40)$$

These common coefficients are discussed elsewhere such as by Yang *et al.* [50]. However, when considering results with finite particle elasticity but no viscoelasticity in the fluid these quantities above are ill-defined (due to a division by zero). So for the complete case where both the capillary number and the Weissenberg number are varied we will discuss the first and second normal stress differences, as opposed to the normal stress normal stress coefficients.

2.5. Mesh and Domain Convergence

There are two main types of convergence that need to be considered for the study of particles in a shear flow while utilizing the immersed boundary method. While the immersed boundary method scales well in particle number and has many advantageous properties, the lack of a body fitted mesh leads to the need for very refined Eulerian meshes

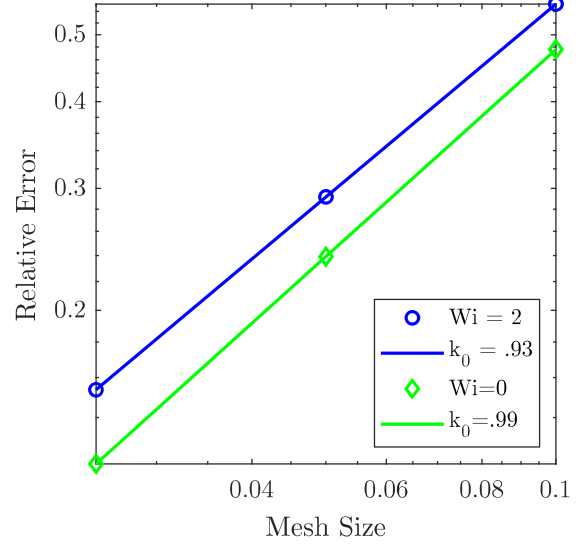


Figure 2: The relative error (error relative to the extrapolated value) in the effective viscosity plotted against the mesh resolution for two deformable particle simulations ($Ca=0.025$) where the Weissenberg number is 2 and 0 on a log-log plot. Solid lines with scalings of .93 and .99 (best fit scalings) are added to guide the eye. Both the high Weissenberg number and the Newtonian case are converging at a nearly linear rate. For the remainder of our simulations we will extrapolate only using the two coarser meshes and use a convergence rate of 1.

for sufficiently converged results. To reduce the need for extremely expensive mesh calculations we utilize Richardson extrapolation to calculate all viscometric quantities presented in this paper. For a generic viscometric ψ we can calculate the approximate rate of convergence for our method, k_0 , using:

$$\psi\left(\frac{h}{t}\right) + \frac{\psi\left(\frac{h}{t}\right) - \psi(h)}{t^{k_0} - 1} \approx \psi\left(\frac{h}{s}\right) + \frac{\psi\left(\frac{h}{s}\right) - \psi(h)}{s^{k_0} - 1}. \quad (41)$$

In the above expression the rate of convergence is k_0 and the three mesh sizes tested are given by h , $\frac{h}{t}$, and $\frac{h}{s}$ where s and t are distinct and larger than 1. We would like to ensure that our method is converging as expected for both a Newtonian case and a chosen high Weissenberg number case since in the simulations we conduct we have both finite fluid elasticity and particle elasticity. We have calculated the rate of convergence defined by Eqn. 41 for a Newtonian suspending fluid and also for a suspending fluid with a $Wi = 2$ and we found the rate of convergence to be .99 and .93 respectively utilizing meshes with 10, 20, and 40 points across the particle diameter. These results for the shear viscosity are presented in Fig. 2 as well as the best fit scalings.

We actually anticipated this nearly linear result since the linear tetrahedral elements utilized in the immersed boundary formulation should produce linear convergence in our problem (despite higher order elements being used in the

fluid solver). We therefore employ a linear convergence rate to extrapolate our results on two mesh sizes and thus calculate the desired viscometric function as:

$$\psi^* \approx \frac{t\psi\left(\frac{h}{t}\right) - \psi(h)}{t - 1}. \quad (42)$$

This procedure is conducted to reduce the number of very costly simulations at a highly refined mesh size. It should be noted that the error that is introduced by assuming the convergence rate is exactly 1 as opposed to .9 or 1.1 introduces an error no larger than 1.5% in the final calculated value. This convergence rate approximation error is thus on the order of errors we make due to the domain size and our threshold for reaching steady state. We utilize boxes that are $5 \times 5 \times 5D_p$ for all of our extrapolations where 10 and 20 points across the particle diameter are utilized.

We additionally need to consider the effect of domain size on the results. We considered box sizes of $5 \times 5 \times 5D_p$ and $10 \times 10 \times 10D_p$ and $20 \times 10 \times 10D_p$ at $Wi=2$ and $Wi=0$ and concluded that no reported viscometrics changed within 2%. The largest errors incurred are generally for the second normal stress differences due to the fact these quantities are very small. We therefore consider a box size of $5 \times 5 \times 5D_p$ to be sufficiently large (volume fraction, $\phi = .0041$) to be simulating the dilute case.

Although the results that we will present are at steady state, the simulations that are conducted are actually transient. We start with the entire domain initially at rest and then at $t = 0$ begin to move the upper and lower walls. When the calculated viscometrics are no longer changing more than 1% over a dimensionless time then the results are considered to be at steady state. These steady state results are then input into the Richardson extrapolation scheme described above.

3. Results and Discussion

3.1. Validation: Newtonian Suspending Fluids with Deformable Solids

The simplest validation case to consider is the case of a single spherical deformable particle suspended in a Newtonian fluid. Previously, Gao *et al.* has considered the analytical solution of this problem and presented the results over a range of capillary number [12]. Below in Fig. 3 the results from a series of our simulations in a domain size of $5 \times 5 \times 5D_p$ are presented. In Fig. 3a the Taylor Deformation parameter (Eqn. 28) is plotted vs. capillary number. Gao's results are presented as a blue dashed line and the simulation results are plotted as open symbols. Additionally, in Fig. 3b the inclination angle is plotted as a function of Ca. In both instances the agreement is good across a range of modest Ca numbers. Notable features in these plots include that the deformation increases nearly linearly with the Ca number (a slightly less than linear deviation can be seen for higher Ca). The inclination angle also gets smaller (the particles turn more into the flow direction) as the Ca increases.

Gao *et al.* also presents the results for the viscometrics as a function of Ca. Below in Fig. 4 the results for the effective viscosity and the first and second normal stress differences are presented as a function of Ca number. Once again the analytical results are presented as a blue dashed line and the simulation results are shown in open symbols. The agreement is again excellent across all parameters presented. Soft particles in a Newtonian flow show decreased effective viscosity as the capillary number increases. This reduction is entirely due to the stresslet since the particle induced fluid stress (PIFS) for Newtonian fluids is always zero. The reduction in the 1-2 component of the stresslet with increased capillary number and thus increased particle deformability is clearly due to the reduced 1-2 component of stress within the particle. The first and normal stress difference both grow nearly linearly in magnitude but have opposite signs. These growing functions can be explained by the increased inclination presented in Fig. 3. As the particle aligns more in the flow the stress differences become more pronounced as the particles principle axes become more aligned with the axes of the flow.

It is worth noting that the results presented above are very insensitive to increased box size (changing by less than 2%). Similar results were seen by Villone *et al.* in their work that includes confinement [47]. Numerically, the parameter $\frac{\lambda_p}{\mu_p}$ maintains incompressibility of the solid if it is set to large values. The results presented above are all insensitive to this parameter except for the inclination angle. It appears that prescribed incompressibility is important to capture the correct inclination angle (i.e. if the parameter is reduced in magnitude the particles incline at a higher angle and thus are less aligned with the flow).

3.2. Validation: Viscoelastic Suspending Solutions with Nearly Rigid Particles

The next validation study we consider is the limit of a nearly rigid particle (i.e. capillary number approaching zero) but suspended in a viscoelastic fluid. The simulations presented below are again for boxes in a domain of $5 \times 5 \times 5D_p$ and at $Ca=0.025$. The results of these simulations are compared to are the dilute results from Yang *et al.* [50]. In this particular case, the viscoelastic fluid will have a mobility parameter $\alpha = 0.015$, and $\beta = 0.69$ as utilized by Yang *et al.* (benchmarked against a real viscoelastic fluid used by Dai *et al.* [6]). Below in Fig. 5, we see that we have again good agreement between our simulations which are presented in open symbols and the data from Yang which is presented as lines.

In Fig. 5a we see the effective viscosity as well as its relative components from the calculations of Yang *et al.* [50] compared to the immersed boundary simulations. The relative viscosity increases overall as viscoelasticity increases, but the stresslet drops while the PIFS increases. We see nearly quantitative agreement with the work of Yang (who utilized body-fitted grids for these simulations). Fig. 5b shows the same comparison for the first normal stress coefficient and Fig. 5c compares the second normal stress co-

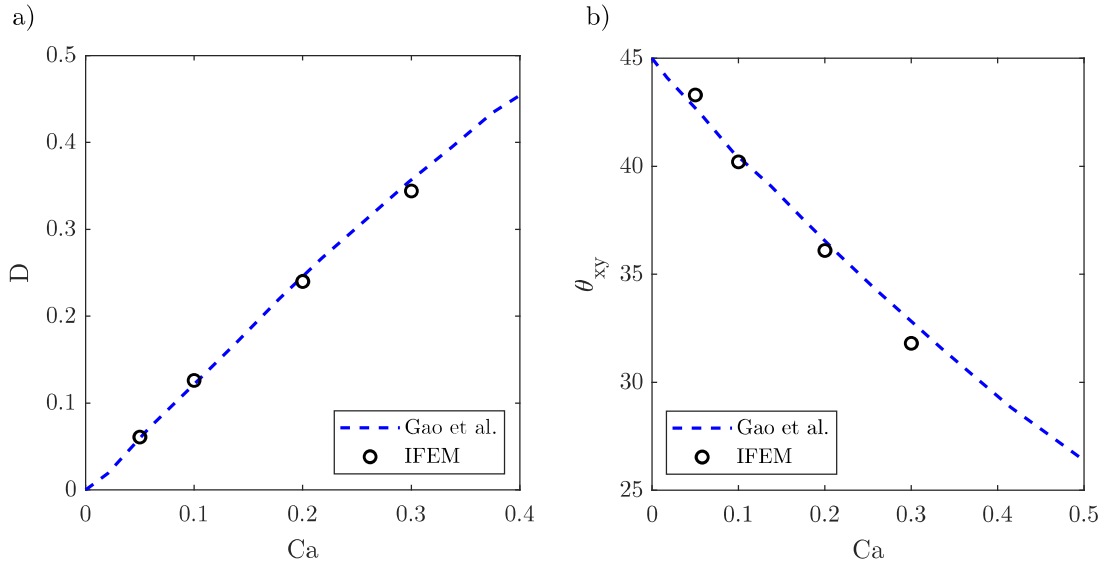


Figure 3: The shape parameters for a dilute sphere in a simple shear flow from our simulations as open symbols as compared to the analytical results by Gao *et al.* presented as dashed lines. [12]. a) We consider the Taylor deformation parameter, D , as a function of Ca . b) We consider the inclination angle, θ_{xy} , as a function of Ca . We see good agreement up to modest Ca numbers. The particles align more heavily in the flow and deform more as the Ca number increases.

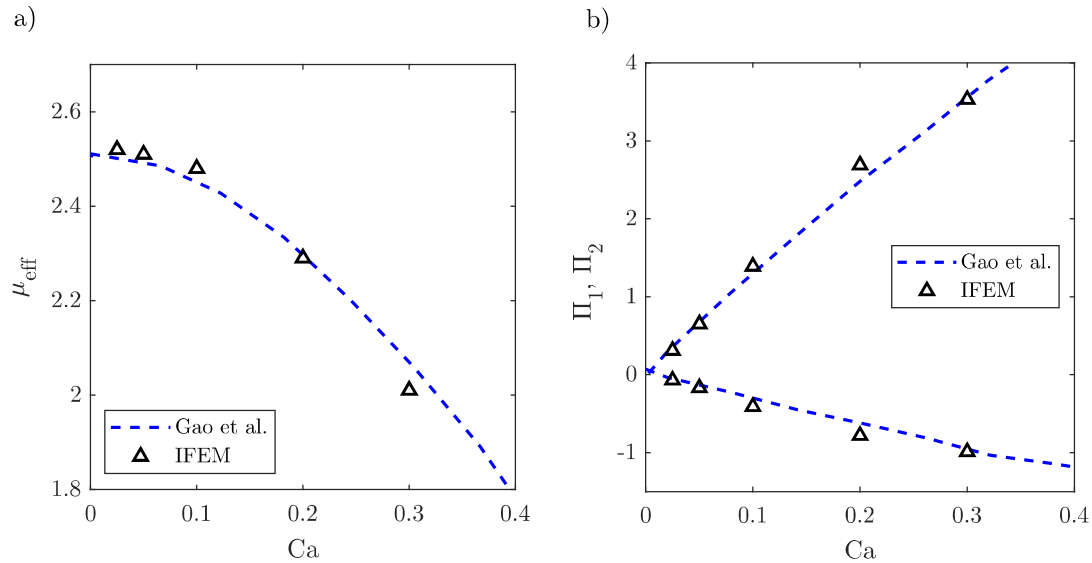


Figure 4: The viscometrics for a dilute sphere in a simple shear flow from our simulations as open symbols compared to the analytical results by Gao *et al.* presented as a dashed line. [12]. a) The effective viscosity as a function of Ca . b) The first and second normal stress differences as a function of Ca . We see good agreement across modest Ca numbers. The particles align more heavily in the flow and deform more as the Ca number increases. This reduces the effective viscosity and increases the magnitude of the normal stress differences as Ca increases.

efficient to our simulations. The normal stress due to the small amount of deformability of the particle at $Ca=0.025$ has been subtracted from the results to test agreement with the rigid result. Again good agreement is seen between the previous results and our work.

3.3. Rheology of a Dilute Suspension of Soft Particles in a Viscoelastic Suspending Media

Next, we consider the problem with both finite deformability (capillary number) and finite Weissenberg number. We know from previous literature and the validation cases presented above that for many of the parameters of interest these

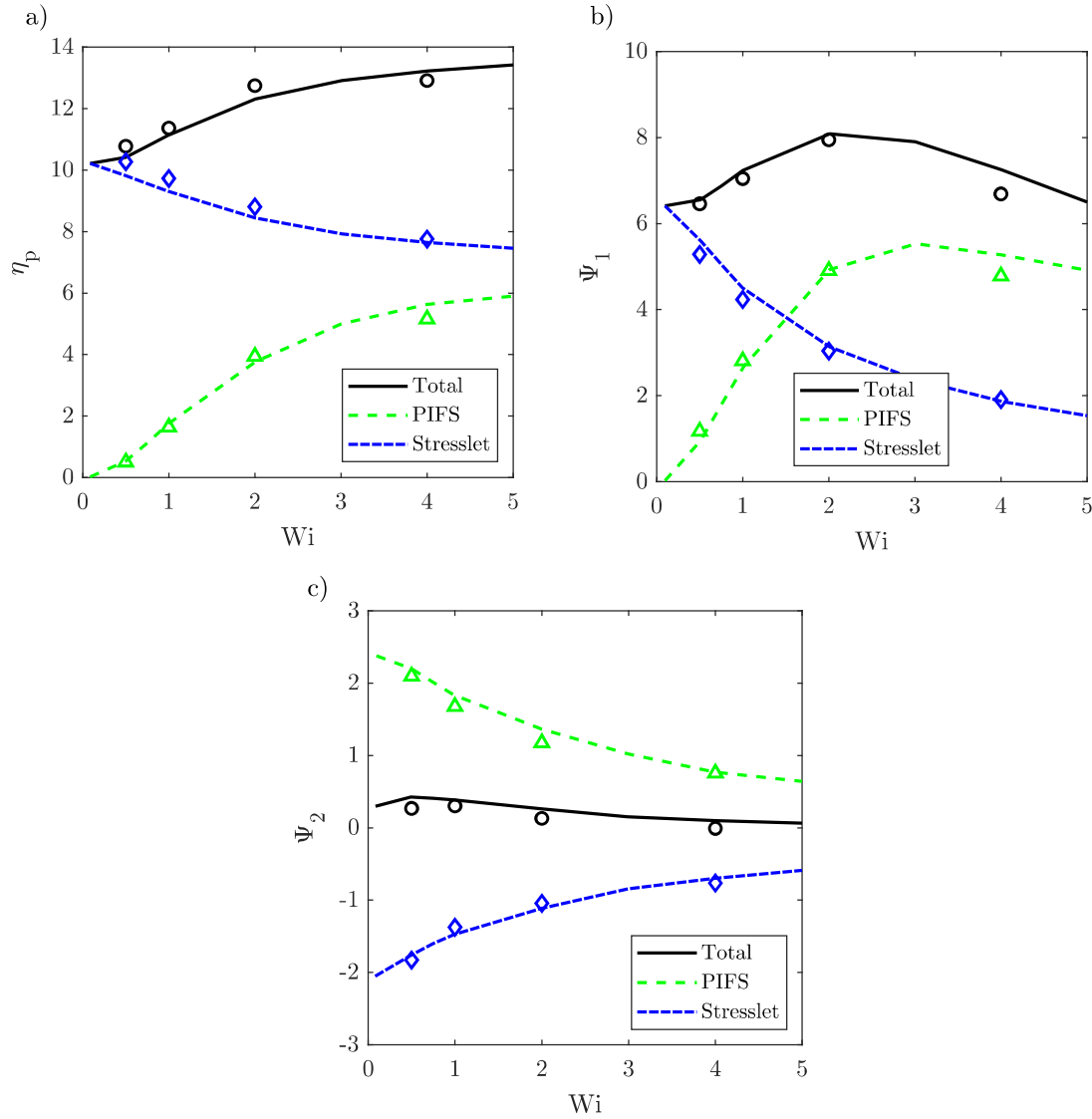


Figure 5: The viscometrics from our simulations ($Ca = 0.025$) as open symbols compared to the results by Yang *et al.* as lines. [50] for nearly rigid particles that are suspended in a viscoelastic media. a) The effective viscosity. b) The first normal stress coefficient. c) The second normal stress coefficient. We have set the Giesekus parameters for these simulations to be $\alpha = 0.0039$ and $\beta = .69$. We see good agreement for all components of the viscometrics including the particle induced fluid stress (PIFS) and the stresslet.

two features are competing with one another. Therefore it will be of interest to see which effect dominates in different flow parameter regimes.

We desire to plot all of our results as a function of one shear rate dependent parameter and a second material parameter (i.e. a dimensionless number that does not depend on shear rate). This presentation will be practically useful since as we vary the shear rate in a realistic experiment (as in a cone and plate or parallel plate rheometer) both the capillary number and the Weissenberg number will be changing simultaneously. However, a material parameter can be defined as constant at the beginning of such an experiment.

We thus define the following dimensionless parameter:

$$\Gamma = \frac{Wi}{Ca} = \frac{\lambda\mu}{\eta}. \quad (43)$$

This parameter is a material parameter and will serve to represent how much elasticity is in the fluid vs. that in the suspended particles.

We will consider the same fluid utilized in the validation study cases: a Giesekus fluid with $\alpha = .0039$ and $\beta = 0.69$. All simulations conducted will be in a box size of $5 \times 5 \times 5 D_p$.

3.3.1. Viscometrics for Different Values of Γ

We consider the effect of viscoelasticity on the three viscometric functions: the per particle effective viscosity and the first/second normal stress differences. In Fig. 6a we see

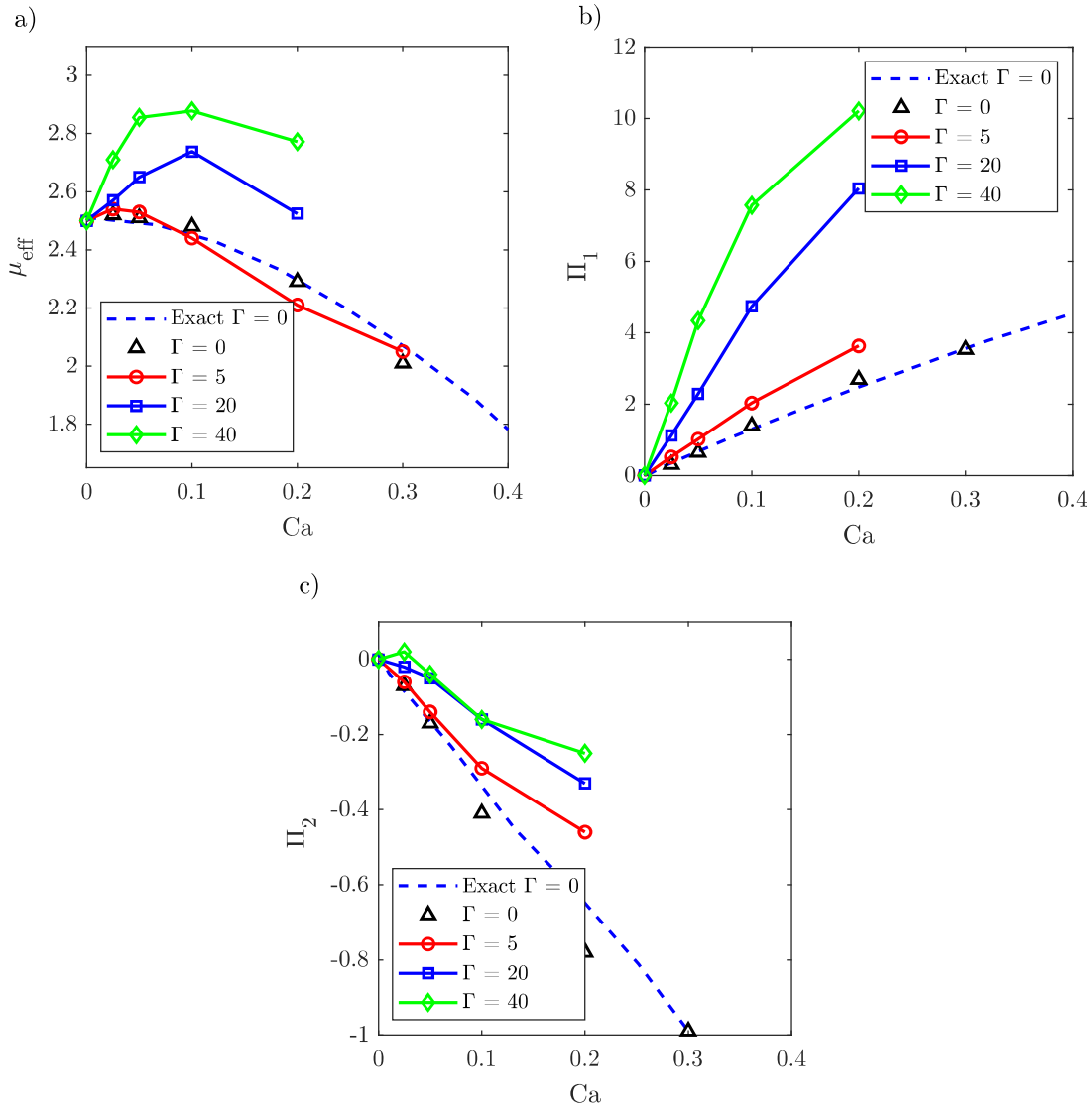


Figure 6: The viscometrics plotted for four values of Γ from our simulations as different open symbols. In a) we plot the per particle effective viscosity vs. the capillary number. We see that the suspensions shear thicken and then proceed to shear thin at higher shear rates. In b) and c) we plot the first and second normal stress differences as a function of Ca. The normal stress differences both become bigger (or become less negative) due to the addition of fluid elasticity. The analytical result for $\Gamma = 0$ from Gao *et al.* is included as a dashed line.

the per particle effective viscosity plotted vs Ca for four different values of Γ . The result for a Newtonian fluid is included as a dashed line from Gao *et al.* We see that the effect of adding fluid elasticity to the problem is for the system to initially shear thicken but then ultimately begin to thin as the shear rate (Ca) becomes higher. This demonstrates that the particle elasticity (i.e. its deformation and internal stress contributions) overcome the effects of the viscoelasticity in the suspending fluid that we have seen is the dominant effect for strictly rigid particles.

It is worth noting that at low but non-zero values of Γ the shear viscosity behaves in a very non-trivial way with multiple inflections in the behavior. This behavior can be broken into three distinct phases. Initially, the system be-

gins to shear thicken. We hypothesize that the fluid elasticity around the particle is leading to increased viscosity similar to that seen for rigid particles since initially the particle will remain approximately spherical. Then a decrease is observed which corresponds to the particle elasticity beginning to appreciably reduce the viscosity of the suspension. The third phase is the subsequent reduction in the thinning slope and is likely due to the increased thickening in the fluid observed as Wi increases (this will be explained more carefully when we consider the PIFS later in this study). This interesting behavior is lost in our calculations at higher Γ since the elastic fluid around the particle has already substantially increased in stress and reached a near maximum before the first thinning inflection. Therefore the higher Γ curves see only

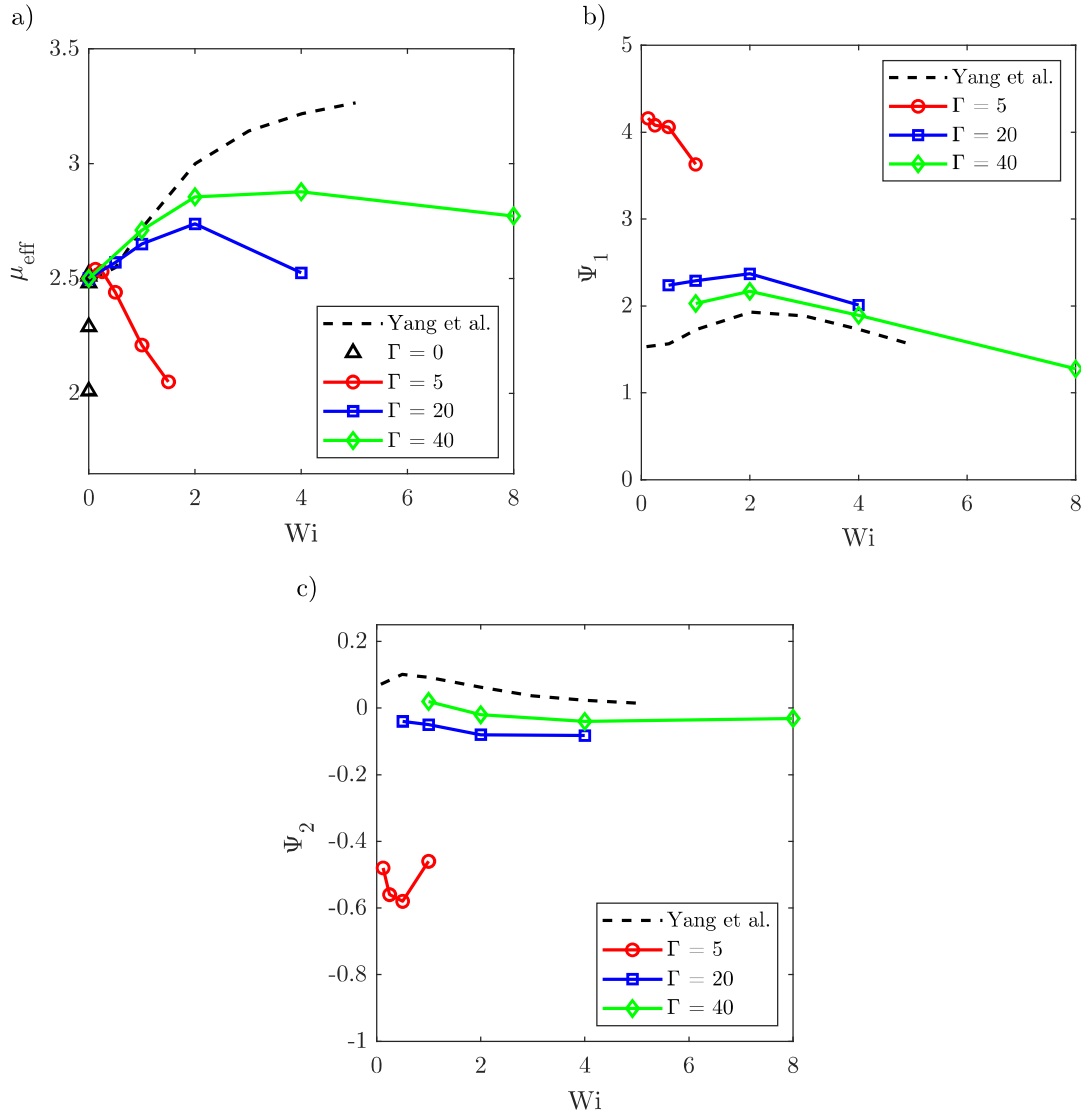


Figure 7: The viscometrics compared to the results by Yang *et al.* [50]. In a) we plot the per particle effective viscosity vs. the Wi number. We see that the suspensions shear thicken and then proceed to shear thin at higher shear rates. In b) and c) we plot the first and second normal stress coefficients as a function of Wi. As Γ approaches infinity we see that the results approach results from Yang *et al.* plotted as dashed lines. Note that in b) and c) to make a comparison to Yang's work we have plotted the normal stress coefficients (normal stresses divided by Wi) to make this comparison where we have previously been discussing normal stress differences.

two distinct phases where the fluid elasticity grows initially and then ultimately decreases due to the particle elasticity at higher shear rates.

In Fig. 6b/c we see the first and second normal stress differences plotted for four values of Γ . Increasing Γ leads to increasing magnitudes of the first normal stress difference and decreasing magnitude of the second normal stress difference. Note that for rigid particles elasticity in the suspending fluid increased first normal stress differences, and we see that fluid elasticity additionally increases the first normal stress difference even more when particle elasticity is considered. The second normal stress differences follow a similar trend where they become slightly less negative. In

our validation calculation, we demonstrated that rigid particles show a slightly positive but small second normal stress so it logically follows that the second normal stress difference would be larger (less negative) when the effect of fluid elasticity is compounded with finite deformability of the particles.

We can also plot these viscometric results against Wi number as opposed to Ca number. This presentation will make the result more comparable to the previous works by Yang *et al.* [50]. Presented in Fig. 7 we see the three viscometrics plotted for varying Γ , but instead as a function of Wi. The results indicate that as Γ gets very large the results of Yang *et al.* (presented as dashed lines) are approached

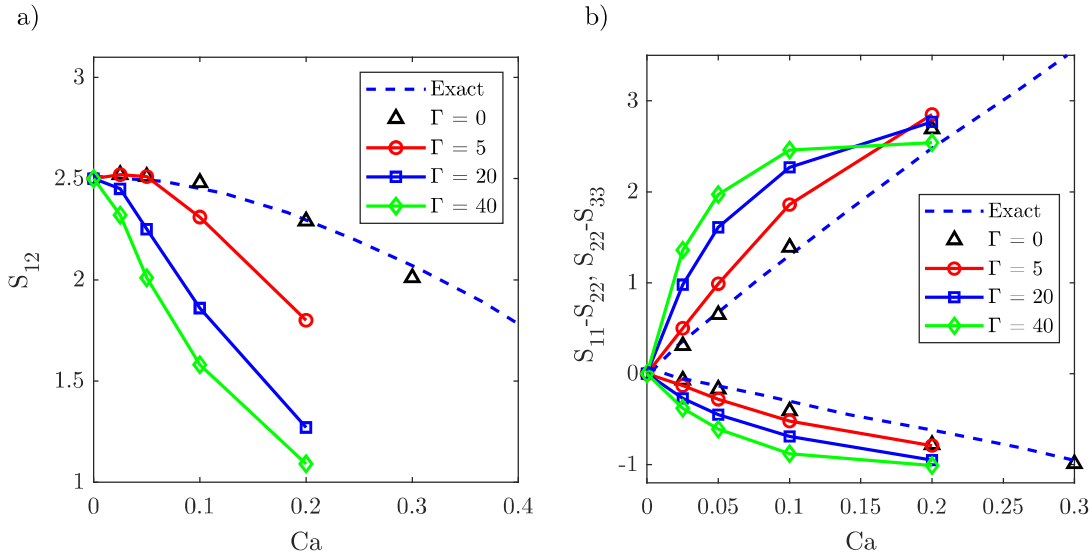


Figure 8: The stresslet contributions to the three viscometric functions as a function of capillary number. The different values of Γ are plotted as different open symbols. a) The stresslet component of the shear viscosity. b) The stresslet contribution to the first and second normal stress differences. We see that as Γ increases that the magnitude of the first/second normal stresses increase and that the magnitude of the shear component decreases rapidly.

(which is sensible since Yang's results represent $\Gamma \rightarrow \infty$).

When discussing the shear viscosity behavior it was proposed that there were distinct regions where the elasticity of the particle and the elasticity of the fluid were competing in determining the rheological behavior. We can quantify these effects by considering the PIFS (Σ) and the stresslet (S) contributions to each of the viscometrics separately. We will first consider the stresslet contribution to the viscometrics and discuss the implications in relation to the total viscometric functions plotted in Fig. 6.

3.3.2. Stresslet Contributions to Viscometrics

As discussed previously, the stresslet quantifies the amount of extra stress is in the suspension due to the stress inside the particle. We can see this from Eqn. 32 rather obviously where the integral over the particle volume has been directly labeled the stresslet.

In Fig. 8 we plot the stresslet contributions to each viscometric against the capillary number for the same four values of Γ that were utilized previously. In Fig. 8a the contributions to the per particle effective viscosity are plotted. We see that the stresslet is the only contributor to the total viscosity for the Newtonian suspension ($\Gamma = 0$). The dashed line indicates the analytical result from Gao [12]. However, as additional suspending fluid elasticity is added to the system the stresslet begins to decrease (i.e. "shear-thin") even faster than the Newtonian case. As was noted in the introduction, these systems of deformable particles with viscoelastic suspending fluids lead to less deformation and more alignment with the flow direction as the Wi increases [48]. This is consistent with what we see in this plot since as the Weissenberg number increases Γ increases, which means we ex-

pect less deformation. For a given particle, if we hold the modulus fixed and decrease the deformation we expect there to be less average stress in the particle and therefore a lower stresslet contribution. Since the reduction in deformation ultimately plateaus at high Wi in all numerical studies to date, it is possible that this effect will converge to a similar slope at higher values of Γ , however, we have not explored this parameter regime.

We can also see the trends for the first and second normal stress differences in Fig. 8b. We see that the magnitude of the stresslet increases relative to the Newtonian case for both the first and the second normal stress differences. This can again be explained by the kinematics of the particles which have been previously discussed in Villone *et al.* [48]. The particles align more with the flow as the Wi is increased and again this effect begins to diminish for very high Wi. This translates into increases in magnitude to the normal stress differences as the principle axes of the particle begin to align with the principle axes of the lab frame. This inclination effect however ultimately plateaus in Wi, so the stresslet contributions to the normal stresses subsequently begin to plateau at high Γ .

3.3.3. PIFS Contributions to Viscometrics

We now will consider the effect that the surrounding fluid has on the the total viscometrics. We will consider the particle induced fluid stress (PIFS) contribution for all three viscometrics, but it should be noted that this integral is not technically just over the fluid for a deformable particle (it actually is for the rigid particle case). The integral presented in Eqn. 33 is actually over the whole domain and includes a term that is the stress inside the particle if the solid actually had

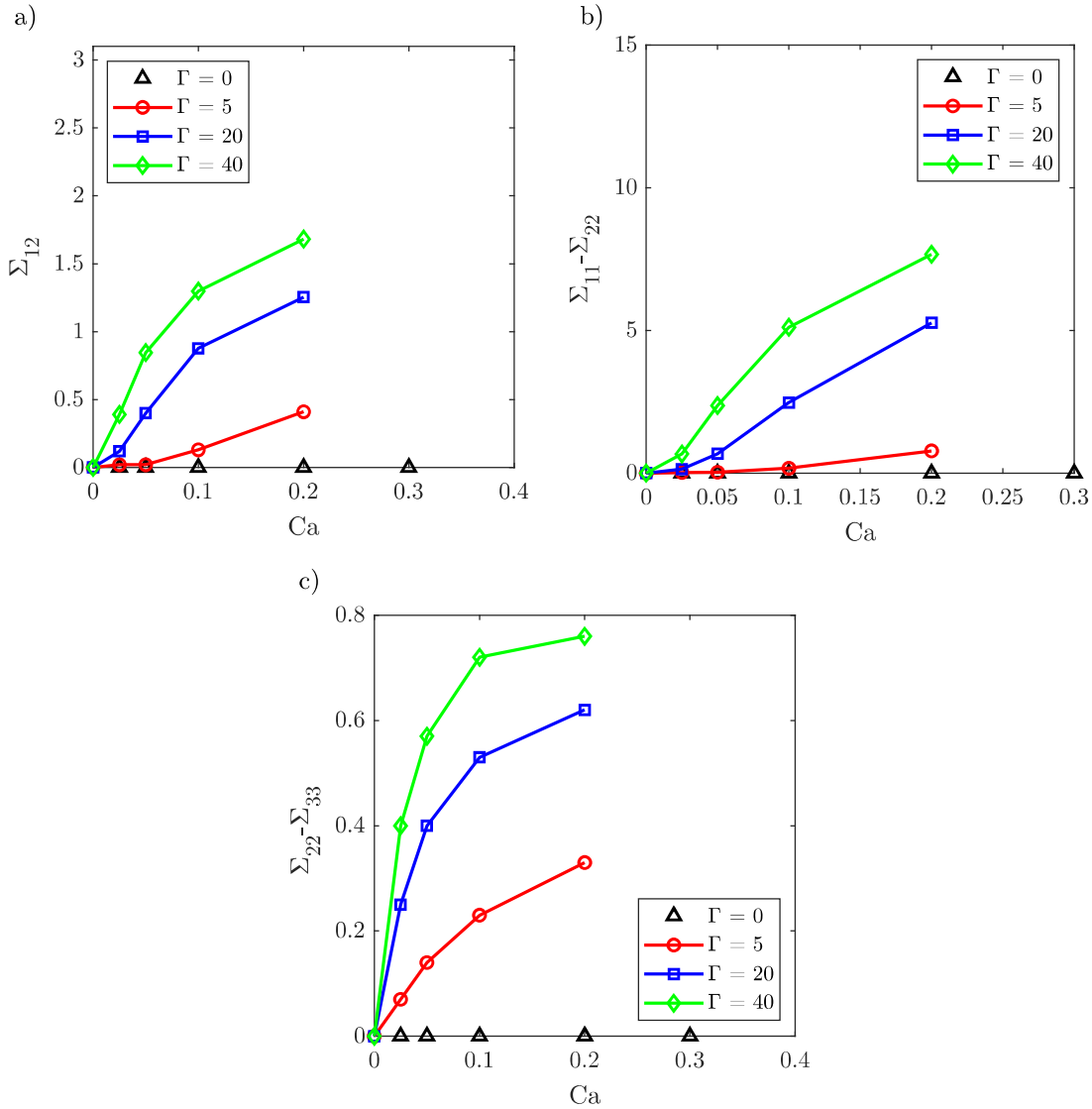


Figure 9: The PIFS component of the three viscometrics plotted as a function of Ca. The different values of Gamma are plotted as different open symbols. a) The PIFS component of the effective viscosity. b) The PIFS component of the first normal stress difference. c) The PIFS component of the second normal stress difference.

a fluid constitutive model. This term is easy to calculate in the immersed boundary method since we already have all of these stresses constructed over the Eulerian domain, but in a body fitted code these stresses would have to be calculated in addition to the ones utilized by the solver. The PIFS term in totality represents how much extra stress is in the fluid surrounding the particle and how much extra stress is produced by particle since it does not follow the fluid constitutive law.

In Fig. 9 we see the PIFS contributions to the three viscometrics. In 9a we see the PIFS contribution to the shear viscosity. It should be noted that for a Newtonian fluid the PIFS is always zero (even for deformable particles). We see that the PIFS increases at a faster and faster rate in Ca as Γ is increased. This is expected since as Γ becomes larger the Wi number grows which means the thickening in the fluid is more pronounced.

In Fig. 9b/c the PIFS contributions to the first and second normal stress differences are shown. Similar trends are seen for both of these viscometrics. The increased value of Γ leads to more and more stress to accumulate in the fluid surrounding the particle.

In the case of the PIFS, we demonstrate a very important collapsing of the data that occurs if we plot the data against Weissenberg number instead of capillary number. In Fig. 10 we see the same data presented in 9 but plotted against Weissenberg number. The collapse in this particular instance is perhaps surprising since this suggests that the extra stress found outside of the particle in the disturbed fluid region is actually not a strong function of the deformed state of the particle (Note the exact opposite result was found for the stresslet contribution).

Previously, Yang *et al.* found that the PIFS term for

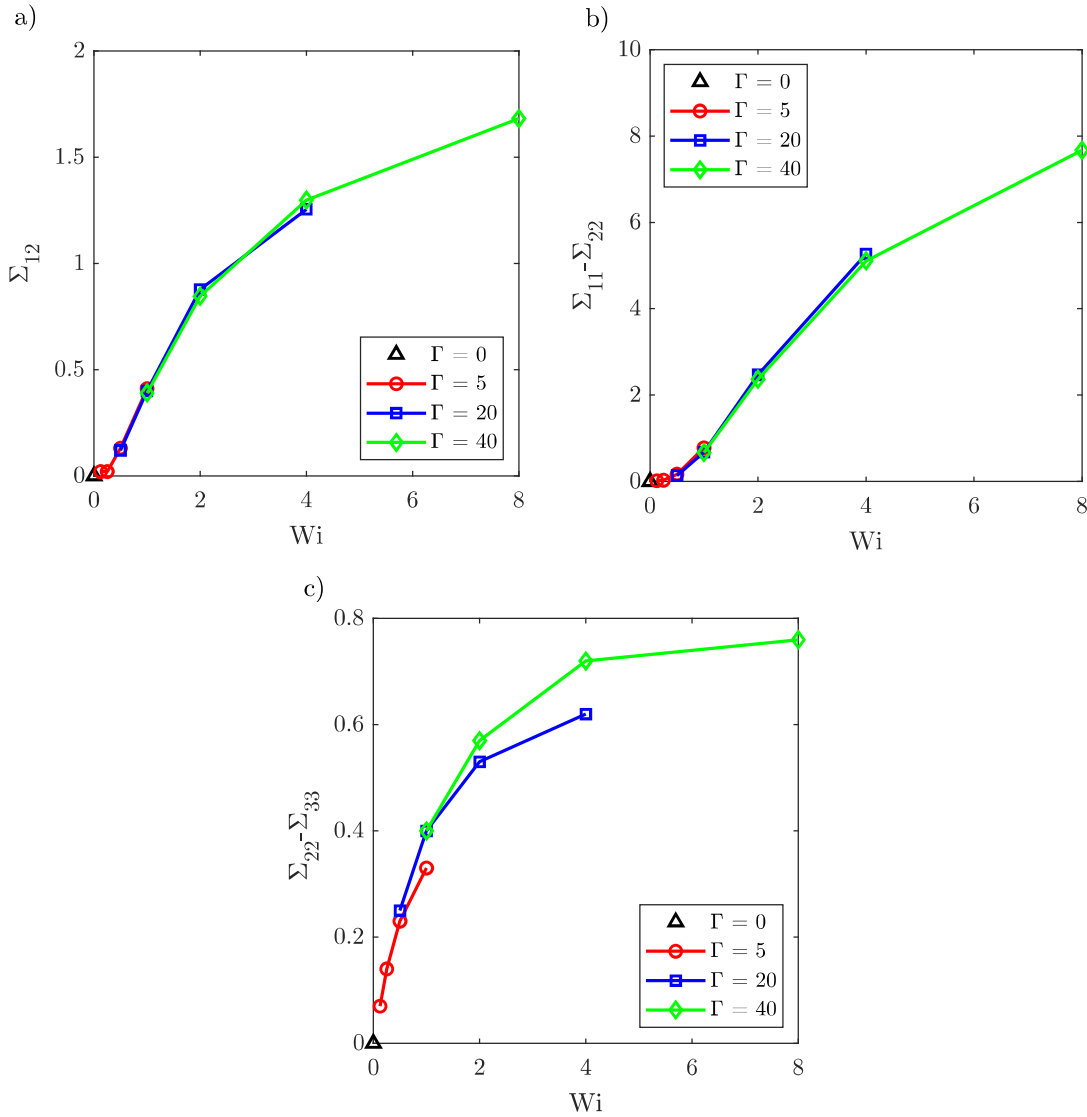


Figure 10: The results for the PIFS component of the three viscometric functions plotted as a function of Wi . The different values of Γ are plotted as different open symbols. a) The PIFS component of the effective viscosity. b) The PIFS component of the first normal stress difference. c) The PIFS component of the second normal stress difference. We see that all of the results collapse onto single master curves when plotted against Wi as opposed to Ca as in Fig. 9. This suggests that the PIFS part of the problem is very insensitive to the Ca number.

rigid particles was due to regions of extreme polymer stress around the particle that did not grow in size with Wi and that these regions of high stress were found in regions of closed streamlines around the particle [51]. In Fig. 11 we see a similar result for our simulations. In panel a) through c) the results for a fixed $Wi=1$ are shown for three different Ca numbers: 0.025, 0.05, and 0.2. The contours plotted are the shear stress in the fluid region outside of the particle. The data collapse suggests that these PIFS regions are all approximately the same at least up to modest $Ca < 0.3$ and we can see this visually in Fig. 11. It is quite surprising even with the relatively substantial deformation illustrated in Fig. 11c that we see a very similar fluid stress profile in the fluid when compared to the nearly rigid particle case. The closed

streamline regions and the extreme stress boundary layers are still present even for the deformable particles and they do not change in a substantial way over the range of parameters considered. In fact, when compared to the results from Yang *et al.* we see that the results presented are in fact in nearly perfect agreement with those from the rigid particle calculations. Fig. 12 shows the collapse of the shear viscosity PIFS calculations to similar results for a rigid particle from Yang *et al.* (adjusted by a factor of $\frac{4\pi}{3}$). This suggests that the PIFS can be understood entirely from rigid particle calculations and thus therefore almost all of the interesting new rheological results are due to the non-linear effects in the stresslet calculations.

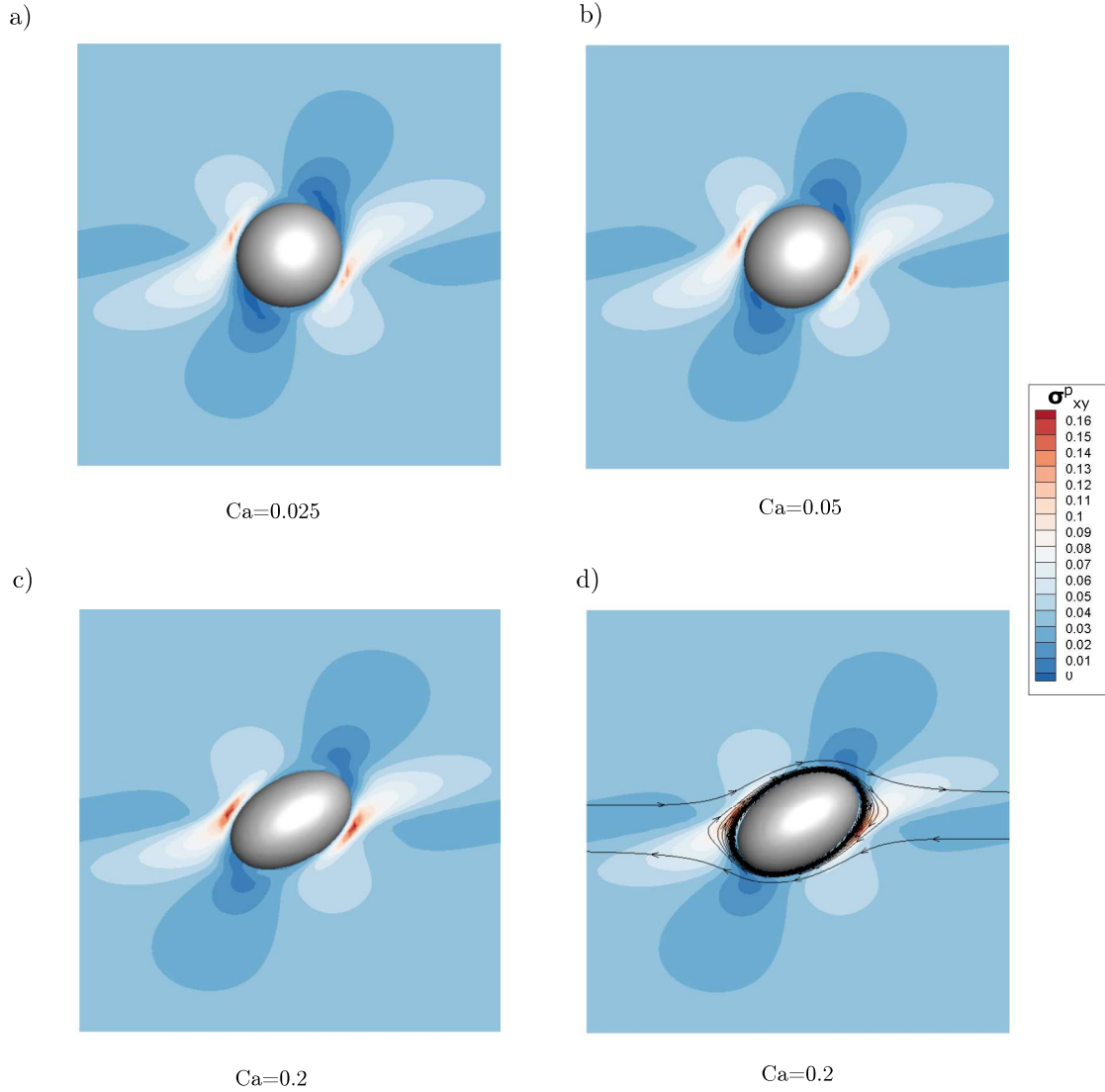


Figure 11: Contour plots of the shear stress component in the fluid. Similar to results by Yang *et al.* [51] we see that the regions of stress in the particle are accumulated close to the particles surface in small regions. The panels a)-c) show the shear component of the stress for 3 different Ca numbers of 0.025, 0.05, and 0.2. Panel d) shows the same plot as panel c) where a select number of streamlines have been added to illustrate that the regions of high stress are within closed streamline regions.

4. Conclusions

The rheology of a dilute suspension of elastic particles in a Giesekus fluid is considered through the use of an immersed finite element method. The method has been validated in both the Newtonian limit against previous work by Gao *et al.* [12] and against the work by Yang *et al.* for dilute suspensions of rigid particles in viscoelastic fluids [50]. Good agreement was found for these test cases across the range of parameters considered.

The results for the rheology of dilute suspensions of elastic particles in Giesekus fluids show an interesting non-linear combination of effects. The particle induced fluid stress (PIFS) is found to be largely invariant to the deformation of the particle (up to $Ca=0.4$) which makes the results presented by

Yang *et. al* [50] concerning particle induced fluid stress for rigid particles largely applicable even when the particle deforms. This indicates that the mechanism indicated by Yang *et al.* is also applicable to elastic particles – i.e. regions of strong stress accumulate near the particle in closed streamline regions in shear flows.

However, the stresslet component of the viscometrics is a strong function of both the viscoelasticity in the suspending fluid and the elasticity of the particle. As viscoelasticity is increased for a given particle deformability the particles aligns in the flow direction and deforms less (as is seen by Villone *et al.* as well [48]). The consequence is the shear component of the stresslet decreases as viscoelasticity of the matrix increases and the stresslet components of the normal stress differences increase as the viscoelasticity increases.

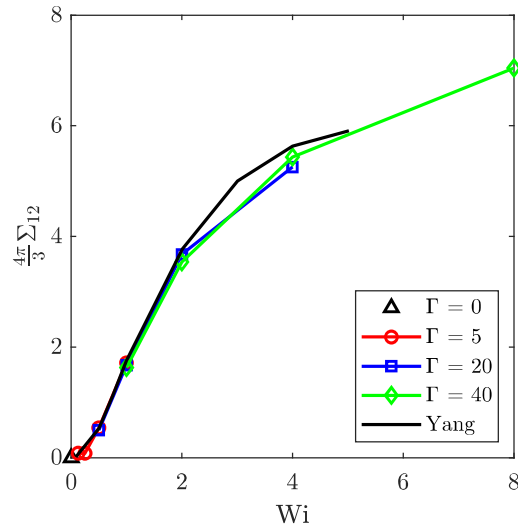


Figure 12: The particle induced fluid stress component of the effective viscosity as a function of Wi for all of the simulations conducted. Different values of Γ are presented as different open symbols. We can see that they collapse well onto a single curve and that this curve corresponds with the result for strictly rigid particles which is illustrated as a solid black line.

These effects are not a simple superposition of the rigid result and the deformable result from a Newtonian flow indicating a substantial non-linear coupling between these effects.

In total the simulations suggest interesting non-linear behavior in the shear viscosity depending on the relative ratio of the elasticity in the fluid to the elasticity in the particle, Γ . The shear viscosity in such a suspension should at first rise, and then rapidly decrease with increasing shear rate. The normal stresses both get larger as elasticity is added to the suspending fluid compared to the Newtonian result. The competition between the two different sources of elasticity and its effect on the stresslet component of the per particle extra stress is the primary component of this new and interesting behavior.

5. Acknowledgments

Funding: This work was supported by the National Science Foundation (CBET-1803765); the US Army High Performance Computation Research Center (W911NF07200271); Computer simulations were also performed on the Stanford University Certainty computer cluster, which is funded by the American Recovery and Reinvestment Act of 2009.

References

- [1] Ardekani, A., Dabiri, S., Rangel, R., 2008. Collision of multi-particle and general shape objects in a viscous fluid. *Journal of Computational Physics* 227, 10094–10107. doi:10.1016/j.jcp.2008.08.014.
- [2] Ardekani, A.M., Joseph, D.D., Dunn-Rankin, D., Rangel, R.H., 2009.

- Particle-wall collision in a viscoelastic fluid. *Journal of Fluid Mechanics* 633, 475. doi:10.1017/S0022112009990632.
- [3] Bagchi, P., Kalluri, R.M., 2009. Dynamics of nonspherical capsules in shear flow. *Phys. Rev. E* 80, 16307. doi:10.1103/PhysRevE.80.016307.
- [4] Bird, R.B., Armstrong, R.C., Hassager, O., 1987. *Dynamics of polymeric liquids. Vol. 1: Fluid mechanics.* Wiley.
- [5] Clausen, J.R., Aidun, C.K., 2010. Capsule dynamics and rheology in shear flow: Particle pressure and normal stress. *Phys. Fluids* 22, 123302.
- [6] Dai, S.C., Qi, F., Tanner, R.I., 2013. Viscometric functions of concentrated non-colloidal suspensions of spheres in a viscoelastic matrix. *Journal of Rheology* 58, 183–198. doi:10.1122/1.4851336.
- [7] D’Avino, G., Hulsen, M.A., Greco, F., Maffettone, P.L., 2014. Bistability and metastability scenario in the dynamics of an ellipsoidal particle in a sheared viscoelastic fluid. *Physical Review E* 89, 043006. doi:10.1103/PhysRevE.89.043006.
- [8] D’Avino, G., Maffettone, P.L., 2015. Particle dynamics in viscoelastic liquids. *Journal of Non-Newtonian Fluid Mechanics* 215, 80–104. doi:https://doi.org/10.1016/j.jnnfm.2014.09.014.
- [9] D’Avino, G., Tuccillo, T., Maffettone, P.L., Greco, F., Hulsen, M.A., 2010. Numerical simulations of particle migration in a viscoelastic fluid subjected to shear flow. *Computers and Fluids* 39, 709–721. doi:10.1016/j.compfluid.2009.11.005.
- [10] Dodd, S.K., Bagchi, P., 2009. Three-dimensional computational modeling of multiple deformable cells flowing in microvessels. *Phys. Rev. E* 79, 46318. doi:10.1103/PhysRevE.79.046318.
- [11] Einarsson, J., Yang, M., Shaqfeh, E.S.G., 2018. Einstein viscosity with fluid elasticity. *Physical Review Fluids* 3, 013301. doi:10.1103/PhysRevFluids.3.013301.
- [12] Gao, T., Hu, H.H., Castañeda, P.P., 2011. Rheology of a suspension of elastic particles in a viscous shear flow. *Journal of Fluid Mechanics* 687, 209–237. doi:10.1017/jfm.2011.347.
- [13] Giesekus, H., 1982. A simple constitutive equation for polymer fluids based on the concept of deformation-dependent tensorial mobility. *J. Non-Newton. Fluid Mech.* 11, 69–109.
- [14] Ham, F., Mattsson, K., Iaccarino, G., 2006. Accurate and stable finite volume operators for unstructured flow solvers. *Annual Research Briefs*, 243–261.
- [15] Izbassarov, D., Rosti, M.E., Ardekani, M.N., Sarabian, M., Hormozi, S., Brandt, L., Tammisola, O., 2018. Computational modeling of multiphase elastoviscoplastic flows. *Int. J. Numer. Meth. Fluids*, 1–23.
- [16] Jaensson, N., Hulsen, M., Anderson, P., 2015. Simulations of the start-up of shear flow of 2D particle suspensions in viscoelastic fluids: Structure formation and rheology. *Journal of Non-Newtonian Fluid Mechanics* 225, 70–85. doi:10.1016/j.jnnfm.2015.09.006.
- [17] Jaensson, N., Hulsen, M., Anderson, P., 2016. Direct numerical simulation of particle alignment in viscoelastic fluids. *Journal of Non-Newtonian Fluid Mechanics* 235, 125–142. doi:10.1016/j.jnnfm.2016.07.008.
- [18] Koch, D.L., Lee, E.F., Mustafa, I., 2016. Stress in a dilute suspension of spheres in a dilute polymer solution subject to simple shear flow at finite Deborah numbers. *Physical Review Fluids* 1, 013301. doi:10.1103/PhysRevFluids.1.013301.
- [19] Koch, D.L., Subramanian, G., 2006. The stress in a dilute suspension of spheres suspended in a second-order fluid subject to a linear velocity field. *Journal of Non-Newtonian Fluid Mechanics* 138, 87–97. doi:10.1016/j.jnnfm.2006.03.019.
- [20] Koch, D.L., Subramanian, G., 2008. Corrigendum to "The stress in a dilute suspension of spheres suspended in a second-order fluid subject to a linear velocity field" [*J. Non-Newton. Fluid Mech.* 138 (2006) 87–97] (DOI:10.1016/j.jnnfm.2006.03.019). doi:10.1016/j.jnnfm.2008.03.005.
- [21] Krishnan, S., Shaqfeh, E.S.G., Iaccarino, G., 2017. Fully resolved viscoelastic particulate simulations using unstructured grids. *J. Comput. Phys.* 338, 313–338. doi:https://doi.org/10.1016/j.jcp.2017.02.068.
- [22] Le, D.V., Khoo, B.C., Peraire, J., 2006. An immersed interface method for viscous incompressible flows involving rigid and flexible boundaries. *J. Comput. Phys.* 220, 109–138. doi:https://doi.org/10.

- 1016/j.jcp.2006.05.004.
- [23] Li, G., McKinley, G.H., Ardekani, A.M., 2015. Dynamics of particle migration in channel flow of viscoelastic fluids. *Journal of Fluid Mechanics* 785, 486–505. doi:10.1017/jfm.2015.619.
- [24] Matsunaga, D., Imai, Y., Yamaguchi, T., Ishikawa, T., 2016. Rheology of a dense suspension of spherical capsules under simple shear flow. *Journal of Fluid Mechanics* 786, 110–127. doi:10.1017/jfm.2015.666.
- [25] Mendez, S., Gibaud, E., Nicoud, F., 2014. An unstructured solver for simulations of deformable particles in flows at arbitrary Reynolds numbers. *J. Comput. Phys.* 256, 465–483. doi:http://dx.doi.org/10.1016/j.jcp.2013.08.061.
- [26] Misbah, C., 2012. Vesicles, capsules and red blood cells under flow. *J. of Phys.: Conference Series* 392, 12005.
- [27] Mittal, R., Iaccarino, G., 2005. Immersed Boundary Methods. *Annual Review of Fluid Mechanics* 37, 239–261. doi:10.1146/annurev.fluid.37.061903.175743.
- [28] Murata, T., 1981. Deformation of an Elastic Particle Suspended in an Arbitrary Flow Field. *Journal of the Physical Society of Japan* 50, 1009–1016. doi:10.1143/JPSJ.50.1009.
- [29] Padhy, S., Shaqfeh, E.S.G., Iaccarino, G., Morris, J.F., Tonmukayakul, N., 2013. Simulations of a sphere sedimenting in a viscoelastic fluid with cross shear flow. *J. Non-Newton. Fluid Mech.* 197, 48–60. doi:https://doi.org/10.1016/j.jnnfm.2013.02.003.
- [30] Peskin, C.S., 2002. The immersed boundary method. *Cambridge University Press*. volume 11 of *Acta Numerica*. pp. 479–518. doi:10.1017/CBO9780511550140.007.
- [31] Pozrikidis, C., 1992. Boundary Integral and Singularity Methods for Linearized Viscous Flow. *Cambridge Texts in Applied Mathematics*, Cambridge University Press. doi:10.1017/CBO9780511624124.
- [32] Pozrikidis, C., 2003. Computational Hydrodynamics of Capsules and Biological Cells. *CRC Press*.
- [33] Raffee, A.H., Dabiri, S., Ardekani, A.M., 2017a. Deformation and buckling of microcapsules in a viscoelastic matrix. *Phys. Rev. E* 96, 32603.
- [34] Raffee, A.H., Dabiri, S., Ardekani, A.M., 2017b. Elasto-inertial migration of deformable capsules in a microchannel. *Biomicrofluidics* 11, 64113.
- [35] Rallison, J.M., 2012. The stress in a dilute suspension of liquid spheres in a second-order fluid. *Journal of Fluid Mechanics* 693, 500–507. doi:10.1017/jfm.2011.544.
- [36] Ramanujan, S., Pozrikidis, C., 1998. Deformation of liquid capsules enclosed by elastic membranes in simple shear flow: large deformations and the effect of fluid viscosities. *J. Fluid Mech.* 361, 117143. doi:10.1017/S0022112098008714.
- [37] Richter, D., Iaccarino, G., Shaqfeh, E.S.G., 2010. Simulations of three-dimensional viscoelastic flows past a circular cylinder at moderate Reynolds numbers. *J. Fluid Mech.* 651.
- [38] Roscoe, R., 1967. On the rheology of a suspension of viscoelastic spheres in a viscous liquid. *Journal of Fluid Mechanics* 28, 273–293. doi:10.1017/S002211206700206X.
- [39] Rosti, M.E., Brandt, L., 2018. Suspensions of deformable particles in a Couette flow. *Journal of Non-Newtonian Fluid Mechanics*.
- [40] Rosti, M.E., Brandt, L., Mitra, D., 2018. Rheology of suspensions of viscoelastic spheres: Deformability as an effective volume fraction. *Phys. Rev. Fluids* 3, 12301. doi:10.1103/PhysRevFluids.3.012301.
- [41] Saadat, A., Guido, C.J., Iaccarino, G., Shaqfeh, E.S.G., 2018. Immersed-finite-element method for deformable particle suspensions in viscous and viscoelastic media. *Physical Review E* 98, 063316. doi:10.1103/PhysRevE.98.063316.
- [42] Scirocco, R., Vermant, J., Mewis, J., 2004. Effect of the viscoelasticity of the suspending fluid on structure formation in suspensions. *Journal of Non-Newtonian Fluid Mechanics* 117, 183–192. doi:10.1016/j.jnnfm.2004.01.010.
- [43] Scirocco, R., Vermant, J., Mewis, J., 2005. Shear thickening in filled Boger fluids. *Journal of Rheology* 49, 551–567. doi:10.1122/1.1849185.
- [44] Sinha, K., Graham, M.D., 2015. Dynamics of a single red blood cell in simple shear flow. *Phys. Rev. E* 92, 42710. doi:10.1103/PhysRevE.92.042710.
- [45] Sugiyama, K., Ii, S., Takeuchi, S., Takagi, S., Matsumoto, Y., 2011. A full Eulerian finite difference approach for solving fluid-structure coupling problems. *J. Comput. Phys.* 230, 596–627. doi:10.1016/j.jcp.2010.09.032.
- [46] Villone, M., D’Avino, G., Hulsen, M., Greco, F., Maffettone, P., 2011. Simulations of viscoelasticity-induced focusing of particles in pressure-driven micro-slit flow. *Journal of Non-Newtonian Fluid Mechanics* 166, 1396–1405. doi:10.1016/j.jnnfm.2011.09.003.
- [47] Villone, M., Hulsen, M., Anderson, P., Maffettone, P., 2014a. Simulations of deformable systems in fluids under shear flow using an arbitrary Lagrangian Eulerian technique. *Computers & Fluids* 90, 88–100. doi:10.1016/j.compfluid.2013.11.016.
- [48] Villone, M.M., Greco, F., Hulsen, M.A., Maffettone, P.L., 2014b. Simulations of an elastic particle in Newtonian and viscoelastic fluids subjected to confined shear flow. *J. of Non-Newton. Fluid Mech.* 210, 47–55. doi:https://doi.org/10.1016/j.jnnfm.2014.05.003.
- [49] Villone, M.M., Greco, F., Hulsen, M.A., Maffettone, P.L., 2016. Numerical simulations of deformable particle lateral migration in tube flow of Newtonian and viscoelastic media. *Journal of Non-Newtonian Fluid Mechanics* 234, 105–113. doi:10.1016/j.jnnfm.2016.05.006.
- [50] Yang, M., Krishnan, S., Shaqfeh, E.S., 2016. Numerical simulations of the rheology of suspensions of rigid spheres at low volume fraction in a viscoelastic fluid under shear. *Journal of Non-Newtonian Fluid Mechanics* 234, 51–68. doi:10.1016/j.jnnfm.2016.04.003.
- [51] Yang, M., Shaqfeh, E.S., 2018a. Mechanism of shear thickening in suspensions of rigid spheres in Boger fluids. Part I: Dilute suspensions. *Journal of Rheology* 62, 1363–1377. doi:10.1122/1.5024696.
- [52] Yang, M., Shaqfeh, E.S.G., 2018b. Mechanism of shear thickening in suspensions of rigid spheres in Boger fluids. Part II: Suspensions at finite concentration. *Journal of Rheology* 62, 1379–1396. doi:10.1122/1.5024698.
- [53] Zhang, L., Gerstenberger, A., Wang, X., Liu, W.K., 2004. Immersed finite element method. *Comput. Meth. Appl. Mech. Eng.* 193, 2051–2067. doi:http://dx.doi.org/10.1016/j.cma.2003.12.044.
- [54] Zhang, L.T., Gay, M., 2007. Immersed finite element method for fluid-structure interactions. *J. Fluids Struct.* 23, 839–857. doi:https://doi.org/10.1016/j.jfluidstructs.2007.01.001.